PAPER www.rsc.org/pccp | Physical Chemistry Chemical Physics

Engineering disorder in precipitation-based nano-scaled metal oxide thin films

Jennifer L. M. Rupp,* Barbara Scherrer and Ludwig J. Gauckler

Received 7th October 2009, Accepted 28th May 2010
DOI: 10.1039/b920971a

Distinctive microstructure engineering of amorphous to nanocrystalline functional metal oxide thin films for MEMS devices is of high relevance to allow for new applications, quicker response times, and higher efficiencies. Precipitation-based thin-film techniques are first choice. However, these often involve organic solvents in preparation. Their relevance on the disorder states of amorphous to fully crystalline metal oxides is unclear, especially during crystallization. In this study the impact of organic solvents on the as-deposited amorphous state and crystallization of the metal oxide, CeO_2, is reported for thin-film preparation *via* the precipitation-based method spray pyrolysis. The choice of organic solvent for film preparation, *i.e.* glycols of different chain lengths, clearly affects the structural packing and Raman bond length of amorphous states. Organic residues act as space fillers between the metal oxide molecules in amorphous films and affect strongly the thermal evolvement of microstructure, *i.e.* microstrain, crystallization enthalpy, crystallographic density, grain size during crystallization and grain growth. Once the material is fully crystalline, equal near- and long-range order characteristics result independent of organic solvent choice. However, the fully crystalline films still show decreased crystallographic densities, presence of microstrain, and lower Raman shifts compared to microcrystalline bulk material. The defect state of amorphous and fully crystalline thin-film microstructures can actively be modified *via* explicit use of organic glycols with different chain lengths for metal oxide films in MEMS.

1. Introduction

Electrically conducting metal oxide thin films are required for quick response and powerful microelectromechanical systems (MEMS). However, there is strong evidence in the known literature that the thermal history of film deposition and post-annealing affect the structural defect states and, consequently, the electrical properties of a metal oxide thin film.[1–3] Their level of disorder is strongly determined by the thin-film preparation method resulting in specific microstructures which may range from amorphous to fully crystalline states. It is reported that their electrical properties scatter widely and differ substantially from microcrystalline bulk for similar materials processed as thin films,[2] *e.g.* ceria-based films show differences up to 30% in their activation energy, several different orders of magnitude in their electrolytic domain boundary and up to one different order of magnitude in total conductivity, depending on the degree of disorder.[1,4] Similar results are also reported for zirconia-[5] and titania-based materials.[2] In general, techniques in the preparation of metal oxide thin films can be separated into two major categories: (i) vacuum-based techniques in which the films are deposited from sintered ceramic pellet targets like pulsed-laser deposition or sputtering,[6] and (ii) precipitation techniques based on aqueous or organic solvents such as spray pyrolysis, sol–gel, spin coating, or chemical vapor deposition.[7,8] The major difference between both classes of these thin-film processing techniques are the degree of disorder introduced during deposition. Whereas atoms are deposited directly from sintered ceramic targets in the case of vacuum-based thin-film methods, metalorganic components are deposited from the precursors for the precipitation thin-film techniques. As a result mostly crystalline films are deposited in the case of vacuum-based thin-film methods and purely amorphous films are deposited for precipitation thin-film techniques.

For MEMS applications precipitation-based thin films are advantageous due to their low-cost and easy upscaling.[9–14] In precipitation-based thin-film methods, the solvent serves as a transport vehicle for the metal salts to direct them onto a heated substrate thus assuring equal distribution for film formation. The metal oxide forms in a single or multiple thermal decomposition steps of the metal salt. Due to the high decomposition temperatures of conventional metal salts, often low-temperature decomposing organic solvents are used in the deposition processes. Residuals of the organic solvents are then present in the amorphous thin films directly after deposition and remain in spite of rather high temperatures of up to 1000 °C in subsequent annealing.[15] As a result, organic solvents may still evaporate and affect the ordering of the atoms of a thin-film during crystallization and grain growth. It is known from literature that organic residues may act as charge-compensators, or space fillers, which may influence the bonding of nearest neighbour ions, or act as participants in hydrogen bonding networks or ligands for completing the coordination around a metal ion.[16,17] Their specific nature depends on the initial near-range order of the metal oxide

Department of Materials, ETH Zurich, ETH Zurich
Wolfgang-Pauli-Str.10, CH-8093 Zurich, Switzerland.
E-mail: jennifer.rupp@mat.ethz.ch

structure, its charge and coordination. Gorbitz and Hersleth classified up to 50 main solvent groups for metalorganic structures capable of affecting crystallization processes.[18] They pointed out that solvents affect, to a large degree, the disorder in the crystalline lattice of the oxide. van der Sluis *et al.* also recognized the importance of understanding the solvent–solute interaction in order to modify actively the crystallization processes of growing crystalline grains in a metal oxide.[19] However, studies of the impact of organic solvents on the near-to-long range ordering of the metal oxide atoms during crystallization and grain growth are lacking, especially for thin films.

In the case of metal oxide powders the effects of organic precursors on their formation and crystallization have been studied. The calcinations and crystallization of amorphous ceria- and zirconia-based particles showed a strong dependency on the organic solvent and aqueous content of the original chemical precursors used in the powder preparations. The crystal growth rates of as-deposited ceria powders from polymeric precursor solutions decreased due to high carbon contents compared to powders prepared from aqueous solutions.[20] In the case of sol–gel derived ceria particles a large impact of the hydroxyl groups on the Ce–O–C bonds and the final crystallite size of the powder was observed.[21] Further, evidence for the important role of organic residues in the crystallization of metal oxides were found: For the crystallization activation energy of 8 mol% yttria-doped zirconia, discrepancies of up to 45% were reported which clearly demonstrate the effect of organic solvents on the defect chemistry of the powders.[22,23]

Recently, we reported on the crystallization and grain growth kinetics of a precipitation-based metal oxide thin-film.[24] These experiments served as a base to establish the first TTT (time-temperature-transformation) diagrams for a metal oxide thin film to predict the proceeding crystallization for integration in MEMS processing routes.[25] In these studies the role of a single-organic-based tetraethylene glycol precursor on the crystallization and grain growth kinetics of an amorphous one-cation metal oxide, CeO_2, was investigated. The grain growth of biphasic films containing amorphous and crystalline phases is driven by the free volumetric enthalpy freed during crystallization of the system. The history of crystallization, *i.e.* isothermal or with respect to temperature, affected the defect and microstrain states during crystallization to full crystallinity.[24,26,27] Within the given material system, it was demonstrated by XRD measurements that microstrain decreases from roughly 7% for the biphasic amorphous–crystalline state to zero strain for annealing to full crystallinity as a function of temperature. Constant microstrain states for the biphasic films were established during these annealings, which relaxed during isothermal crystallization to reach a constant strain state. Large microstrains around 3% after relaxation were present for fully crystalline films annealed at a relatively low temperature of 600 °C after 10 h of dwell. Parallel to decreasing microstrain, a crystallographic density increase of up to 14% was reported during crystallization. The organic precursor, a glycol, was found likely to affect crystallization kinetics, but its specific role was not clarified. Typically, glycols are first choice over low-boiling point ethanols, methanols, or propanols for sol–gel or pyrolysis processes.[28] State-of-the-art glycols used for precipitation-based film processing are diethylene glycol ($O(CH_2CH_2OH)_2$) and tetraethylene glycol ($O(CH_2CH_2OCH_2CH_2OH)_2$). The latter glycol features almost double the chain length and, thus, a high boiling point of 330 °C compared to diethylene glycol with a boiling point of 245 °C. It is important to note that the choice of organic solvent strongly affects the thin-film deposition temperature to produce continuous films without cracks in precipitation-based methods.[8,29,30]

In this current paper, the impact of chain length of organic solvent on the initial as-deposited amorphous state of ceria films prepared *via* spray pyrolysis is reported. The role of the organic solvent residues on crystallization kinetics and on the microstructure of the final fully crystalline film are discussed in relation to annealing temperature. Two state-of-the-art glycols for precipitation-based processes, *i.e.* tetraethylene and diethylene glycols, are used as solvents in the preparation of ceria films. For the first time the near- and long-range disorder evolvement is discussed by comparing X-ray diffraction (XRD), differential scanning calorimetry (DSC) and Raman investigations for the amorphous state, during crystallization and of a fully crystalline metal oxide thin-film with respect to its organic solvent used in preparation. Finally, conclusions are presented for actively modifying the disorder states of amorphous to fully crystalline metal oxide films by the choice of organic solvent in film preparation for MEMS.

2. Experimental

Thin-film preparation

Two different ceria spray pyrolysis precursor solutions were made with 0.1 mol L^{-1} cerium nitrate (Alfa Aesar, 99% purity) dissolved either in 10 : 90 vol% water and tetraethylene glycol (TEG) (Aldrich, > 99% purity), or 10 : 90 vol% ethanol and diethylene glycol (DEG). The precursor solutions were fed into a spray gun (Compact 2000 KM, Bölhoff Verfahrenstechnik, Germany) with a liquid flow rate of 5 ml h^{-1} and atomized at 1 bar air pressure on a heated sapphire single crystal substrate (Stettler, Switzerland). Depending on the type of the precursor, the substrate temperature and spray time were 315 ± 5 °C for 1 h or 390 ± 5 °C for 1.45 h for 1 : 9 ethanol : DEG or 1 : 9 H_2O : TEG, respectively. The working distance between the spray nozzle and the hot plate was kept at 39 cm during all experiments. The spray pyrolysis process is described in further detail elsewhere.[7–9] After spray pyrolysis film deposition, the thin films were amorphous and could be converted to biphasic amorphous–nanocrystalline or totally nanocrystalline films by annealing at temperatures higher than the spray pyrolysis deposition temperature.[10,11]

Microstructure

Top-view microstructures of the thin films were characterized using scanning electron microscopy (SEM, Zeiss Leo 1530, Germany). Prior to imaging, the thin films were sputtered (Bal-Tec, SCD 050, Sputter Coater) with a Pt coating in order to avoid charging and to allow imaging at higher resolutions.

Chemistry

The chemical compositions of the films were determined by energy-dispersive X-ray spectroscopy (EDX, Leo 1530, Germany) using the cerium L-line at 20 kV.

Crystallization

Crystallization of the amorphous spray pyrolysis thin films during annealing was measured in calibrated differential scanning calorimetry (DSC/TG, Netzsch STA 449C) experiments for 3 °C min^{-1}. The degree of crystallinity from the exothermic heat loss signal and the amount of amorphous *versus* crystalline phase can be determined from the experiments.[31] In order to quantify the DSC results, the instrument was calibrated with calibration standards (Netzsch 6.223.5-91.2) of known melting points and heat losses, or phase changes. Then, as-deposited amorphous CeO_2 thin films were scratched off from the sapphire substrate and the powder obtained was analyzed by DSC. The powder was always enclosed in a Pt pan with lid and measured against an empty Pt pan with lid as a reference under static air atmosphere.

For continuous heating, 50 ± 1 mg of amorphous CeO_2 powder was measured at heating rates of 3–20 °C min^{-1}. A subsequent correction measurement for quantitative DSC analysis using a totally crystallized CeO_2 spray pyrolysis powder of the same mass at equivalent experimental conditions was performed. The signal of this experiment was recorded and subtracted from the measurement of the originally amorphous powder.

Grain growth

The average grain size was determined by X-ray diffraction (XRD, Bruker AXS D8 Advance). The development of line widths of the Bragg peaks during *in situ* annealing in a furnace (Anton Paar HTK 1200) provided information on the average grain size development. Diffracted X-rays from the sample were recorded by a position sensitive detector (Braun PSD ASA-S). The XRD setup was equipped with a copper radiation source (λ = 0.15404 nm), operated at 40 kV and 40 mA and followed by a $K\alpha_1$-Ge monochromator (Bruker AXS). The average grain size was determined from the full width at half maximum (FWHM) by using Fourier analysis of the XRD peaks, refined by a split Pearson 7 function (Software EVA 6.0). The FWHM results from instrumental broadening and microstructure. The instrumental peak broadening of the diffractometer was determined by measuring a commercially available microcrystalline and stress-free CeO_2 powder of large particles (Alfa Aesar, purity 99.99%). The instrumental broadening can be eliminated from the FWHM using the Warren and Biscoe equation.[32] Average grain size, crystallographic density, and microstrain were calculated according to the Scherrer and Wilson equation.[33,34] For experimental details on the latter see ref. 24.

Raman spectroscopy

Raman spectra were recorded by using a spectrometer (Witec, Ulm, Germany); a HeCd laser with an excitation wavelength of 442 nm was used in a macromode.

3. Results and discussions

3.1 Microstructures

The impact of the organic solvent—diethylene glycol (DEG) or tetraethylene glycol (TEG)—on the microstructure of deposited CeO_2 thin films on sapphire substrates is shown in the SEM top-views of Fig. 1. Thin films shown in Fig. 1a and b were deposited from an organic precursor with DEG at 315 °C, and those in Fig. 1c and d with TEG at 390 °C substrate temperature. Note that the substrate temperatures are adjusted to the relative boiling points of the glycols in order to allow continuous crack-free films (see also ref. 29 and 30). All other parameters were kept constant during spray deposition of the films.

As-deposited thin films exhibit, independent of the original precursor, crack-free, dense and smooth microstructures (Fig. 1a and c). Grains with globular shapes connected by straight grain boundaries develop while heating to 1000 °C (Fig. 1b and d). The TEG-based films show in general slightly larger grains compared to DEG-based ones. The latter microstructures show smaller grains due to a lower deposition temperature and solvent boiling point. These are strongly related in spray pyrolysis film formation, since crack-free microstructures can only be assured in the case of a deposition temperature lowered by 60–80 °C with respect to solvent boiling point of the initial precursor.[35]

Typical film thicknesses were 300 ± 30 nm measured by SEM cross-sections as reported in a previous study.[24] EDX analysis revealed the presence of pure ceria for all thin films investigated under this study.

3.2 Crystallization

The mass loss and crystallization monitored by the DSC and TG signals of as-deposited CeO_2 films made from DEG- and TEG-based spray precursors are shown in Fig. 2.

All films in DSC investigations show a pronounced endotherm with maxima shifting from 90 to 120 °C with increasing heating rate (Fig. 2a and c). In this temperature range the films lose most of their mass (around 3 wt%), which is attributed to the desorption of water (see TGs in Fig. 2b and d). Mass losses continue with 1.5–2 wt% until 530 °C. These losses were monitored as outgassing water and carbon, *i.e.* residues of the organic precursor solvents, by mass spectrometry used during the spray pyrolysis processes. In the case of the TEG-based films mass loss terminates at around 530 °C, whereas DEG-based films show an on-going mass loss of 0.2 wt% up to 950 °C. Table 1 summarizes the total mass losses of the films.

In parallel to the recorded weight losses between 400 and 950 °C, broad exotherms are monitored for all films by DSC. These are attributed to the transformation of an amorphous into a crystalline phase of the films and are proportional to the crystallization enthalpy of the material, as shown previously.[13] Since crystallization starts above 400 °C in all DSC spectra, it can be concluded that the as-deposited films are amorphous, independent of their precursor. This is in agreement with previous XRD and DSC studies on TEG-based ceria films.[24]

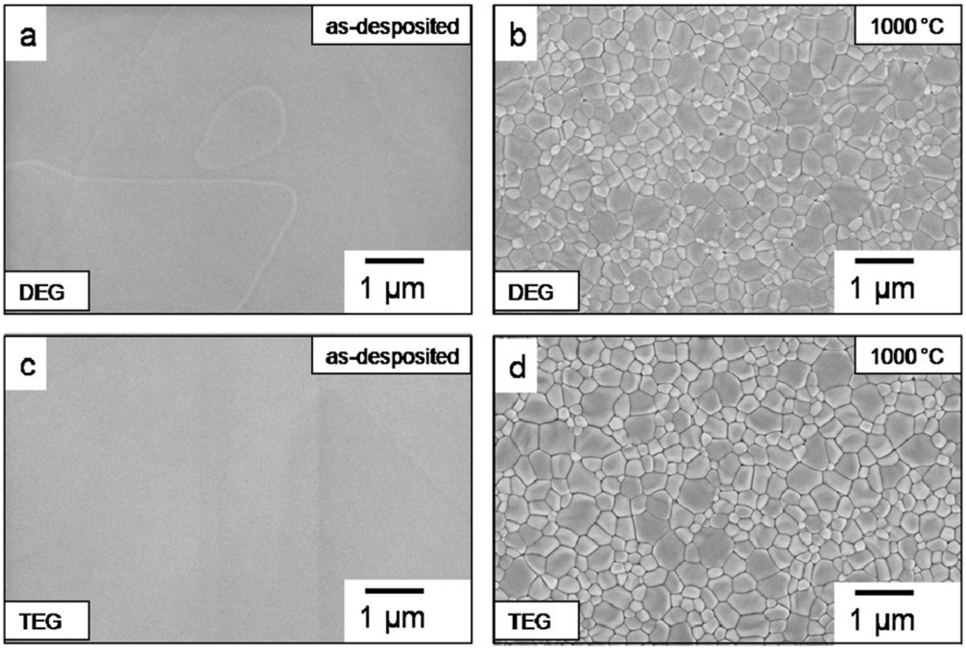

Fig. 1 SEM micrographs of spray pyrolysis CeO_2 thin films on a sapphire substrate with respect to different organic solvents, *i.e.* diethylene (DEG) and tetraethylene glycols (TEG), for the precursors used for film deposition. Annealing films are shown for DEG (a) as-deposited and (b) after annealing at 1000 °C for 0 h, and for TEG (c) as-deposited and (d) after annealing at 1000 °C for 0 h. Except for the glycols and deposition temperatures, all other spray parameters were kept equal during film depositions. Films were always heated with ± 3 °C min^{-1} heating and cooling rate.

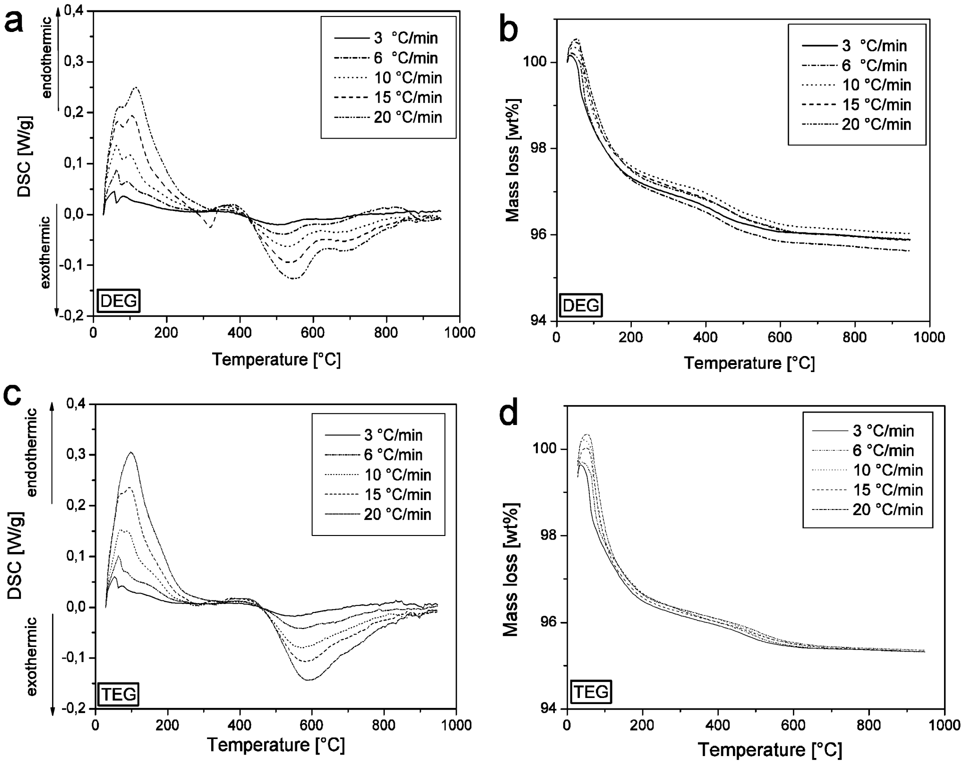

Fig. 2 DSC and TG of spray pyrolysis CeO_2 thin films on sapphire substrate with respect to different organic solvents—diethylene (DEG) and tetraethylene glycols (TEG)—for the precursors used for film deposition. For the DEG-organic prepared films: (a) DSC and (b) TG are shown, and for the TEG-organic solvent prepared ones: (c) DSC and (d) TG are displayed. Except for the glycols and deposition temperatures all other spray parameters were kept equal during film depositions. Films were always heated with ± 3 °C min^{-1} heating and cooling rate.

Table 1 Total weight loss of as-deposited ceria spray pyrolysis thin films as measured by TG in the temperature region 20–950 °C with respect to initial organic solvent, *i.e.* diethylene (DEG) and tetraethylene glycol (TEG), for the precursor and deposition temperature, quantified from Fig. 2

	Total weight loss (wt%)	
Heating rate/°C min^{-1}	DEG solvent Substrate temperature: 315 °C	TEG solvent Substrate temperature: 390 °C
3	4.27	4.53
6	4.58	4.60
10	4.32	5.14
15	4.59	4.93
20	4.64	5.23

In Fig. 3 the detailed analysis of the exothermic crystallization enthalpy, ΔH_{cryst}, and crystallization peak temperature, T_p, are given. Ceria films show, independent of their precursors, a crystallization enthalpy in the temperature range 400–950 °C. The crystallization enthalpy of DEG-based films is characterized by two overlapping peaks, the first between 400–630 °C and a second weaker one between 630–950 °C. A single crystallization peak is monitored in the case of TEG-based films.

Crystallization peak temperatures show a typical kinetic dependence on heating rate, but more interesting is the strong dependence on the organic glycol type used in the preparation (see Fig. 4). The DEG-organic solvent-based films exhibit two crystallization peak temperatures, $T_{p,1a}$ and $T_{p,1b}$, around 500–540 °C and 650–695 °C for heating rates of 3–20 °C min^{-1}, respectively. Contrarily, crystallization of TEG-organic solvent-based films reveals an intermediate and single crystallization peak temperature in the range 540–590 °C. In Fig. 5 the crystallization enthalpies are summarized. The TEG-organic solvent-based films always show a 12% lower crystallization enthalpy than the DEG ones.

In Fig. 6 the crystallized fractions were resolved with respect to temperature and heating rate by integral fractions of the exotherm representing the crystallization enthalpies of the material. A sigmoidal shaped curve is obtained for both types of films. This is similar to classical glass-ceramics transition typically described by the Johnson-Mehl-Avrami model.[14] The linear correlation between crystallized fraction and temperature holds for the main part of the crystallization process, and the two non-linear parts reflect the nucleation and the end of crystallization for the material.[36]

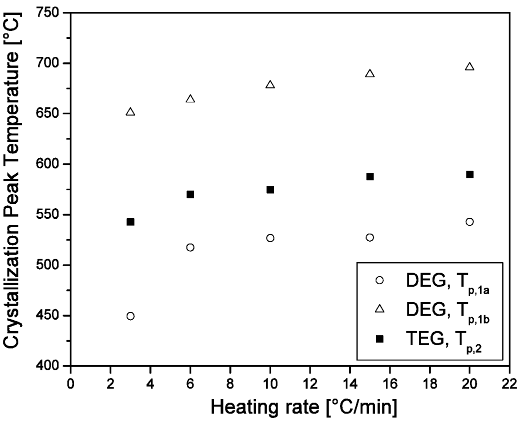

Fig. 4 Non-isothermal crystallization peak temperature of CeO_2 produced by spray pyrolysis with respect to the different organic solvents, *i.e.* diethylene (DEG) and tetraethylene glycols (TEG). Data are derived from Fig. 3.

Nucleation phase, indicated by the non-linear correlation between the crystallized fraction and temperature, proceeds within a very short temperature interval between 400–460 °C for both types of films. For the DEG-based precursor material a two-stage crystallization is found reflected by two linear crystallization slopes. One slope and, therefore, a single crystallization process characterizes the TEG-based films.

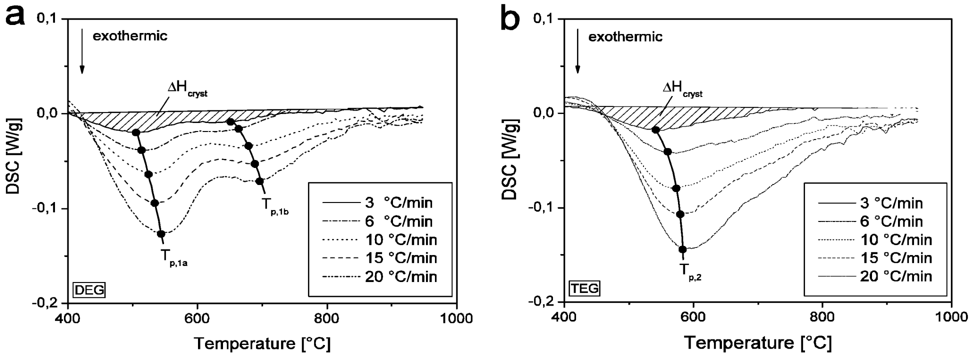

Fig. 3 Exothermic DSC heat release attributed to crystallization of CeO_2 produced by spray pyrolysis with respect to different organic solvents, *i.e.* diethylene (DEG) and tetraethylene glycols (TEG): (a) DEG and (b) TEG. The crystallization enthalpy is denoted as ΔH_{cryst} and the crystallization peak temperature as T_p. Except for the glycols and deposition temperatures all other spray parameters were kept equal during film depositions.

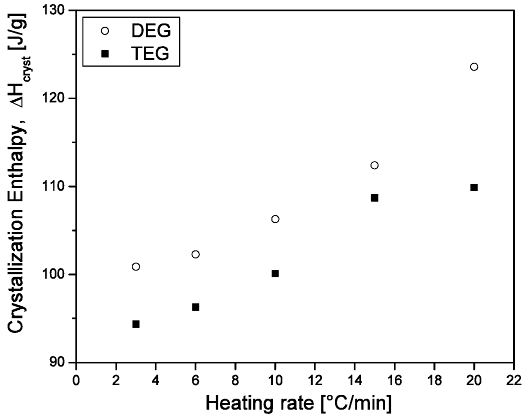

Fig. 5 Non-isothermal crystallization enthalpy of CeO$_2$ produced by spray pyrolysis with respect to different organic solvents, *i.e.* diethylene (DEG) and tetraethylene glycols (TEG). Data are derived from Fig. 3. The crystallization peak temperature is denoted as T_p. Except for the glycols and deposition temperatures all other spray parameters were kept equal during film depositions. The crystallization enthalpy is denoted as ΔH_{cryst}.

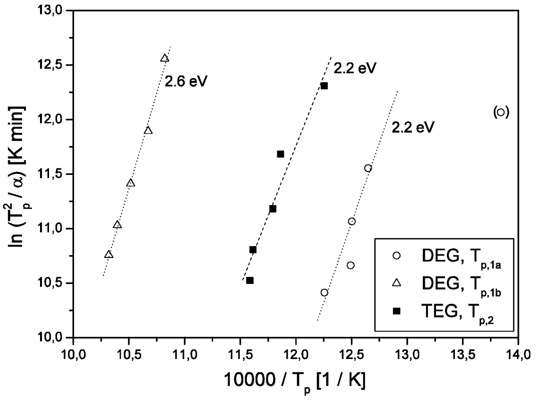

Fig. 7 Kissinger plot of CeO$_2$ produced by spray pyrolysis with respect to different organic solvents, *i.e.* diethylene (DEG) or tetraethylene glycols (TEG), at film deposition. The crystallization peak temperature is denoted as T_p. Except for the glycols and deposition temperatures all other spray parameters were kept equal during film depositions.

Crystallization accomplishes at around 950 °C independent of the precursor.

Activation energies can be obtained from the Arrhenius plot of the Kissinger equation[16] shown in Fig. 7 for the thermally activated crystallization processes (E_a):

$$\ln\left(\frac{T_p^2}{\alpha}\right) = \frac{E_a}{RT_p^2} + \text{const.} \qquad (1)$$

where, R is the gas constant, T_p the crystallization peak temperature, and α the heating rate. Activation energies are 2.2 eV for the first crystallization process independent of the choice of glycol in the film preparation. It is interesting to note that equal activation energies are measured for this first crystallization process, even though the actual crystallization peak temperatures are dependent on the organic solvent of film preparation. The additional second crystallization process for the DEG-based films is characterized by a larger activation energy of 2.6 eV. Differences of up to 1.1 eV were reported in ref. 22, 23 and 37 for zirconia-yttria sol–gel films dependent on the original organic solvents and residual amounts of hydroxyl groups. Hence, activation energy changes through different glycols for pyrolysis preparation of the present films are not so pronounced.

The following conclusions can be made concerning crystallization with respect to temperature:

(i) The organic residues are incorporated into the amorphous metal oxide structure, affecting its future crystallization history. It is driven by the ability to lose organic residues and, thus, promote the closer packing of atoms in the lattice of the material. Once the total weight loss *via* outgassing organic residues is accomplished, ceria remains fully crystalline.

(ii) The short-range ordering of the amorphous states is dependent on the organic solvent choice in the preparation process. Otherwise, no impact on crystallization would be measurable.

(iii) The overall crystallization enthalpies depend strongly on the initial solvent preparation, and deposition temperatures. It is to be emphasized that strong differences of up to 12% were measured for the crystallization enthalpy depending on the choice of glycol for film preparation. Kissinger activation energies may very well characterize the outgassing of

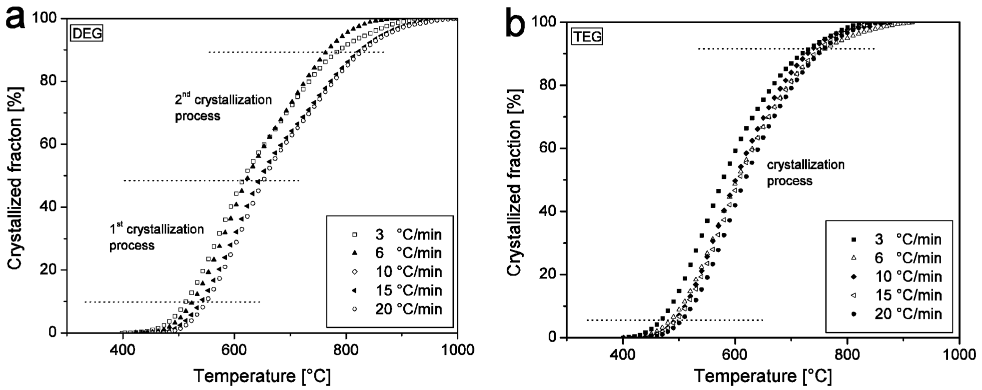

Fig. 6 Non-isothermal crystallized fraction of CeO$_2$ produced by spray pyrolysis as function of different organic solvents, *i.e.* diethylene (DEG) and tetraethylene glycols (TEG), for film deposition. Data are derived from Fig. 3. Except for the glycols and deposition temperatures all other spray parameters were kept equal during film depositions.

different organic residues during crystallization through their specific activation energies.

3.3 X-Ray density and microstrain

The crystallographic packing densities and microstrain were determined by XRD measurements for the deposited ceria thin films. In Table 2, the data are compared with respect to degree of crystallinity as determined by DSC and to the organic solvent involved in the film preparation. Thereby, the microstrain characterizes the long-range correlated displacement field that extends throughout grains of a material.[38] XRD patterns are reported in detail elsewhere.[24]

The amorphous ceria films have an X-ray density of 5.53 and 5.94 g cm^{-3} for the DEG- and TEG-organic solvent prepared films, respectively, as determined from the XRD reflection peaks. The packing density increases with proceeding crystallization of the material. For the fully crystalline films a crystallographic density of 7.2 g cm^{-3} was measured independent of initial film processing.

In the case of the TEG-organic solvent based films, microstrain was analysed. The biphasic amorphous films with 5% of crystalline phase as determined by DSC show 2.51% of microstrain, whereas fully crystalline films revealed no measurable microstrain by X-ray diffraction.

It is remarkable that the X-ray density of the amorphous ceria films exhibits a strong dependence on the length of the glycol used in film preparation. The DEG-prepared thin films show roughly 9% lower packing density relative to the higher boiling point TEG organic solvent prepared films. Organic residues are incorporated more in a ceria spray pyrolysis thin film with the shorter the glycol length and the lower the film deposition temperature.

Heating and crystallization to 500 °C results in a strong increase of the packing density with a 25% increase in case of the biphasic thin films with 5% of crystallized phase for TEG-based film preparation (see Table 2). A comparison of the present microstrain value around 2.5% for CeO_2 to earlier investigations on $Ce_{0.8}Gd_{0.2}O_{1.9-x}$ spray pyrolysis thin films with a similar degree of crystallinity reveals that the present microstrain is lowered by roughly 60%.[26] The lowered microstrain may reflect a lower degree of disorder as no extrinsic dopant is present.

The fully crystalline thin films exhibit a strong increase in crystallographic density of 7.2 g cm^{-3}. Once crystallization of the material is accomplished a processing-independent crystallographic density is measured for the material. However, it is surprising that the crystallographic density of the fully crystalline thin films is still substantially lower when compared to macrocrystalline powders with a density of 7.67 g cm^{-3} with grains in the micrometre range.[39] In contrast to the differing densities of fully crystalline films *versus* macrocrystalline powders, one can confirm that in both cases a zero measured X-ray microstrain resulted.

3.4 Raman shift

The first-order Raman spectra of CeO_2 are displayed in Fig. 8 for the as-deposited and 1000 °C annealed thin films for the two organic solvents used in the preparation. The as-deposited films are amorphous, whereas the annealed ones are fully crystalline according to the results of the previous crystallization study by DSC. All thin films are characterized by a single and high Raman peak maximum situated between 458 and 463 cm^{-1}. The peak shapes show peak asymmetry independent of their degree of crystallinity or the organic solvents used in the preparation. The asymmetry of the Raman line shape is most pronounced for the amorphous films when compared with the spectra of the crystalline thin films.

The Raman shifts and full width at half maximum (FWHM) are displayed in Fig. 9 with respect to the degree of crystallinity taken from the DSC data for these films. The fully crystalline CeO_2 thin films reveal equal Raman shifts with 462.7 cm^{-1} and FWHM around 14.9 cm^{-1} independent of their film preparation. By contrast, a strong dependence of the Raman modes is quantified for the amorphous states, *i.e.* Raman shifts of 458.6 and 461 cm^{-1} with FWHM of 24.8 and 21.8 cm^{-1} were determined for the DEG- and TEG-based organic based films, respectively. It is remarkable that an up to 4 cm^{-1} Raman shift between the amorphous and fully crystalline microstructural state of the CeO_2 films are evident.

The measured Raman peak can be ascribed to the single active triply degenerate F_{2g} Raman mode of CeO_2 for all films.[39] This Raman mode refers to the symmetric stretching mode of the Ce–O8 units.[40] Macrocrystalline CeO_2 powder exhibits a symmetrical Gaussian peak form with a maximum

Table 2 Near- and long-range order of CeO_2 spray pyrolysis thin films for amorphous, biphasic, and fully crystalline states with respect to organic solvent used in the film preparation, *i.e.* diethylene (DEG) and tetraethylene glycol (TEG). Represented by Raman shifts of F_{2g} stretching mode, crystallographic density, and microstrain. Thin-film data are compared to macrocrystalline powder in ref. 39

			Raman bond length of Ce–O8 (F_{2g}) mode			
Spray pyrolysis: precursor organic of thin films	Annealing after film deposition/°C	Degree of crystallinity	Raman shift/cm^{-1}	FWHM/cm^{-1}	Crystallographic density/g cm^{-3}	Microstrain (%)
DEG (substrate T = 315 °C)	None	Amorphous	458.58	24.797	5.53	(Infinite)
	500	Biphasic: amorphous-crystalline (Crystalline phase = 5%)			6.07	
	1000	Fully nanocrystalline	462.75	14.834	7.20	—
TEG (substrate T = 390 °C)	None	Amorphous	461.08	21 832	5.94	(Infinite)
	500	Biphasic: amorphous-crystalline (Crystalline phase = 5%)	461.15	18 997	6.33	2.51
	1000	Fully nanocrystalline	462.76	15 002	7.20	0
Macrocrystalline powder	—	Fully crystalline	465.50	9.86	7.65	(0)

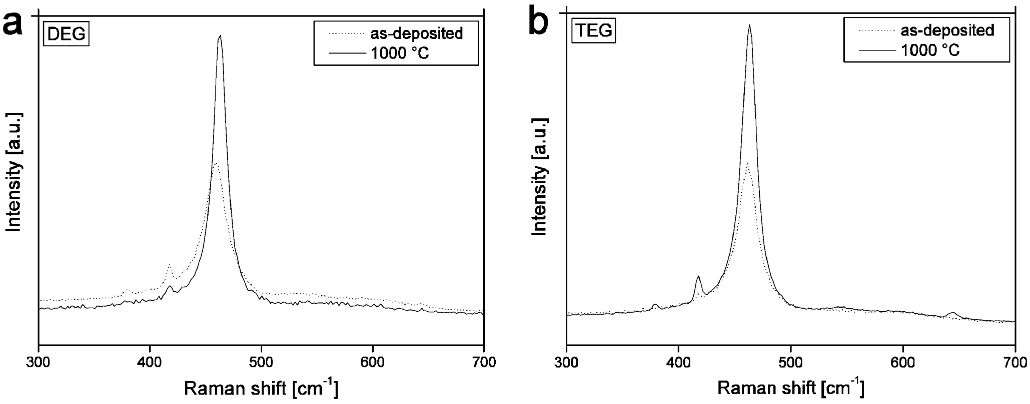

Fig. 8 Raman spectra of the F_{2g} stretching mode for spray pyrolysis ceria thin films in relation to the organic precursor, *i.e.* diethylene (DEG) and tetraethylene glycols (TEG), used in film fabrication. As-deposited films were amorphous, whereas 1000 °C annealed ones exhibited fully crystalline microstructures. Heating to fully crystalline films was performed with 3 K min^{-1}. Except for the glycols and deposition temperatures all other spray parameters were kept equal during film depositions.

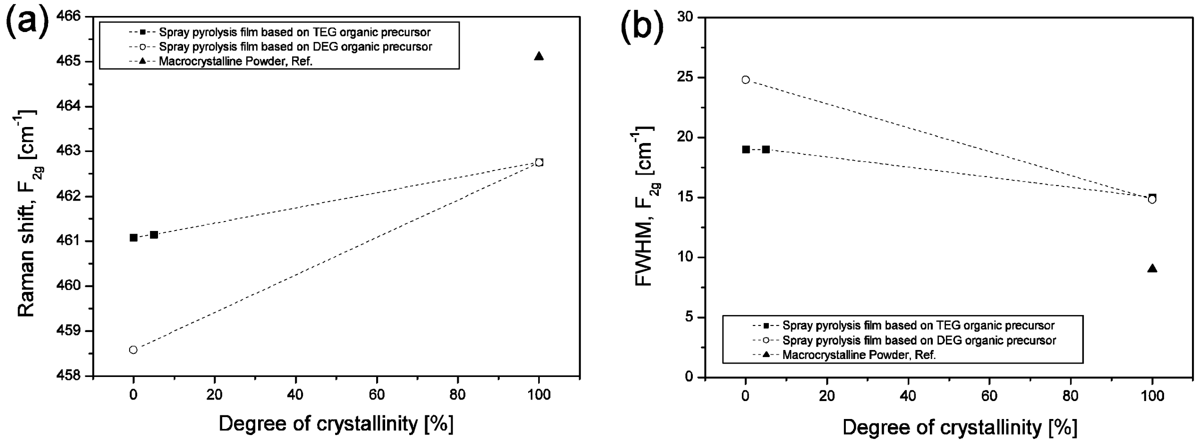

Fig. 9 Raman shift and full width of half maximum (FWHM) of the F_{2g} stretching mode for spray pyrolysis ceria thin films dependent on the organic precursor, *i.e.* diethylene (DEG) and tetraethylene glycol (TEG), used in film fabrication and as a function of the degree of crystallinity. Except for the glycols and deposition temperatures all other spray parameters were kept equal during film depositions. For the purposes of comparison thin-film data are compared to microcrystalline ceria powders from ref. 39.

around 465 cm^{-1} and a FWHM of 9 cm^{-1}.[39] Contrarily, all thin films show an asymmetric Lorentzian Raman line profile, decreased Raman F_{2g} shift, and larger FWHM in this study.

The amorphous films reveal the highest asymmetric peak shape and red shifts of up to 7 cm^{-1} compared with macrocrystalline CeO_2 particles, as seen in Fig. 8. This strong red shift is relatively large and comparable to that observed for 1–20 mol% extrinsic doping of the materials with a cation of the lanthanide group elements (*i.e.* Nd[41] or Sm[42]) or, for example, Fe.[43] Remarkably, the present red shifts of the amorphous ceria thin films are especially sensitive to the organic glycol used in film preparation. Raman shifts up to 2.5 cm^{-1} exist among the amorphous films. Lowest Raman shift and broadest FWHM exist for the low-boiling point DEG organic solvent.

The strong differences in the F_{2g} stretching modes among the amorphous ceria films signify the different near-order states of the material with respect to the glycol choice for the precursor in preparation. Amorphous ceria incorporates different residues from the organic solvents in its structure dependence on the organic glycol used in the preparation. It is known from catalysis literature that incorporation of carbon into ceria particles results in pronounced red shifts of the Raman F_{2g} shift and increased asymmetry of the peak shape.[44] It is interesting to note that the same Raman characteristics are measured for the ceria films with the organic residues.

Once crystallization has been accomplished and fully crystalline films exist, a processing-independent Raman shift at 462.7 cm^{-1} and a FWHM around 14.9 cm^{-1} is characteristic. The Raman shifts are still lowered by 2.5 cm^{-1} and the FWHM increased by 50% for these fully crystalline films when compared to macrocrystralline powders. It can be concluded that the fully crystalline spray pyrolysis CeO_2 thin films exhibit a lower lattice packing relative to standard macrocrystalline powders resulting in the stronger red shifts of the F_{2g} stretching mode.

All films show Lorentzian Raman line profiles with higher peak asymmetries towards smaller Raman shifts. In general, several factors like microstrains, defects and variations in phonon relaxations with decreasing particle size can contribute to these peak form changes and affect the line width and peak position.[45] Asymmetric line shapes and lowered Raman shifts were reported for CeO_2 F_{2g} Raman modes for nanocrystalline powders,[41,46–49] as well as for precipitation-based nanocrystalline thin films.[50,51] It was shown in the literature that asymmetric line profiles and FWHM widening of the F_{2g} Raman mode is due to microstrain, whereas the peak position is determined by the grain size for ceria.[41,52] Spanier *et al.* reported asymmetric line shapes and FWHMs up to 15 or even 30 cm^{-1} as a result of microstrain for nano-CeO_2 particles.[52] These reported FWHMs fully agree with our Raman findings for the ceria thin films in this study. The strongly broadened FWHMs, as well as the Lorentzian asymmetric peak forms, clearly confirm the presence of microstrain in the material.

It can be concluded that the fully crystalline spray pyrolysis CeO_2 thin films exhibit a stronger degree of microstrain and disorder relative to standard macrocrystalline powders which persists even though crystallization has clearly been accomplished. Strong variations in Raman peak FWHM among the amorphous films are interpreted as different microstrain and disorder states of the materials. Amorphous films show a strong dependence on the organic solvent chosen for film preparation in contrast to fully crystalline films or macrocrystalline powders.

To what extent the present microstrain-disorder state of a metal oxide may generally be quantified *via* Raman spectroscopy remains to be discussed. Gouadec *et al.* emphasize that the Raman stretching modes such as the F′ modes characterize local crystal fields only, and more specifically the short-range order to the next nearest neighbours.[45,53,54] Long-range disorder is not characterized by these Raman F′ modes. It was further specified that the measured microstrain *via* Raman of fully crystalline ceria materials characterizes the inhomogeneous strain distribution due to dispersion in grain size and defects.[41,52] Therefore, it is reasonable to ascribe the asymmetric Raman line shapes and broadened FWHMs of the measured F_{2g} mode of ceria films to inhomogeneous strains which are probably enriched in the near grain boundary area. However, for quantification of microstrain states locally resolved X-ray analysis would be required.

In the known literature it has been argued that widening of lattice constants and Ce–O bonds may result from changes in nonstoichiometry.[41–43] An additional Raman peak around 599 cm^{-1} for partially reduced nanocrystalline powder samples due to extrinsic oxygen vacancies was reported.[55,56] This Raman mode is very sensitive to changes in the nonstoichiometry due to a close phonon coupling to the oxygen sublattice of a ceria-based material. Since only a single active Raman shift is present for the present ceria thin films, variations in nonstoichiometry cannot be confirmed.

4. Disorder on short *versus* long range

Structural disorder state of metal oxide thin films are important for understanding ionic and electronic conductions in the future. Short- and long-range disorder is discussed and summarized for ceria spray pyrolysis thin films.

Amorphous ceria thin films differ strongly in their short range order from well crystallized material. The atomic bonding to the next nearest neighbours and their structural packing are strongly dependent on film processing, and especially on the organic solvent. Residues from glycol organics of the precursors are differently incorporated into the metal oxide structure, acting as space fillers between the forming metal oxide bonds.

Raman allows for investigation of the near-range order of amorphous ceria films through shifts and peak widths. The different incorporation of organic residue within the amorphous ceria films is confirmed by wide variations in Raman shifts F_{2g} mode position up to 3 cm^{-1}, and relative changes of FWHM up to 12%. The asymmetric Lorentzian peak shapes and widened FWHMs compared to macrocrystalline material result from strong phonon displacement and confirm the high degree of disorder in these structures. As a consequence nearest neighbour bonds are large and a loose structural packing persists.

X-Ray analysis of the amorphous structures results in low structural packing densities compared to microcrystalline material. Up to 7% difference in packing density can be confirmed for the ceria thin films with respect to the glycol type involved in the film preparation. This confirms the low and varying degree of ordering in the amorphous state. This further supports Raman results that organic residuals from film processing are clearly incorporated within the amorphous metal oxide structure. Loose packing of the metal oxide film was observed *via* Raman and XRD for the DEG organic solvent preparation route relative to the TEG preparation. This signifies that the choice of glycol length has to be taken into account for film preparation. The choice affects the local bonding and, hence, degree of disorder within the metal oxide through space filling with organic residues.

In the case of biphasic ceria films with low amounts of crystalline phase of around 5%, an increase of crystallographic density and Raman shift towards slightly higher modes with narrowing of peak width were measured. The latter peaks are characterized by a decreased FWHM and decreased peak asymmetry compared to the amorphous states.

The study of short-range order *via* Raman reveals qualitatively that inhomogeneous microstrain fields exist in a metal oxide through asymmetry of the Raman line and broad FWHMs. However, quantification of microstrain levels of the material is not possible for ceria since its Raman F′ mode contains only local bonding information. A long-range study *via* X-ray diffraction is required to quantify the microstrain states of biphasic amorphous-crystalline metal oxides (see ref. 24 and 26 for details). The reason is that microstrain fields usually extend over many metal-oxide bonds in the microstructure and interact on a long-range, even though they are accumulated in the near-grain boundary areas of growing grains.[38] In this study we confirm a microstrain around 2.5% for these biphasic TEG-based films from the X-ray diffraction study. This is comparable to microstrain levels in other metal oxides, *i.e.* doped ceria.[24,26]

In the known literature on glass and glass-ceramics, the Raman modes may be used for quantification of the degree of crystallinity of the material.[45,57] A linear correlation between total Raman peak shift between amorphous and crystalline state is used to quantify the degree of crystallinity for glass-ceramics. This can be done as long as the assumption holds that the F′ Raman mode positions only characterize the local bonding and contain no long-range information. Analysis of the Raman shifts results in a degree of 4.2% crystallinity for the TEG-organic solvent-based ceria thin films annealed at 500 °C. This is in agreement with the DSC study of exothermal heat release, showing around 5% crystallinity. Therefore, we suggest, especially for biphasic metal oxide thin films crystallizing in cubic crystal symmetries, Raman analysis of F′ modes for a quick access of the degree of crystallinity as a considerable approach. However, further materials' data on other oxide systems are required full assurance that the degree of crystallinity is affecting the Raman shifts only for metal oxide films.

The fully crystalline thin films show equal Raman shifts and peak widths independent of the preparation, *i.e.* the choice of organic solvent. Once the material is fully crystalline, no dependence on the organic solvent used in film processing is detectable *via* Raman spectroscopy. It is surprising that even though the film has reached full crystallinity, typical Raman shifts, FWHM or Gaussian peak symmetry of a macro-crystalline material have not been reached. This shows that Raman is, in the case of ceria, capable of showing that the material is not fully strain-free by its Raman line anisotropy and strong FWHM broadening. Locally, microstrain states still vary and are qualitatively well captured by Raman measurements.

A strong narrowing of the X-ray diffraction peak width is measured for the fully crystalline materials. Obviously, X-ray diffraction peak width analysis does not capture the residual disorder characterized by Raman. Therefore, Raman analysis is first choice for qualitative evaluation of microstrain presence in fully crystalline ceria thin films.

5. Conclusions

In this study, we have shown for the very first time that the choice of organic solvent strongly determines the near-range order of amorphous CeO_2 thin films made by precipitation method. The organic residues act as space fillers within the amorphous metal oxide thin-film structure and affect its subsequent crystallization history. During crystallization the degree of microstrain and disorder of the material depends on the initial choice of organic solvent, *i.e.* glycol type, and deposition temperature in film preparation. The overall crystallization enthalpies depend on the initial organic solvent choice. The latter crystallization enthalpies can differ by up to 12% depending on the glycol choice. Once the material is fully crystalline the near- and the long-range order characteristics still differ from state-of-the-art microcrystalline bulk material through their stronger degree of disorder by lower packing densities, widened and red-shifted Raman bond lengths, and measurable residual microstrain in the near grain boundary areas as confirmed by Raman spectroscopy.

From the strong difference in the disorder state between fully crystalline ceria thin films and microcrystalline bulk material we may expect differences in the electrical conduction properties. One can reasonably assume that current differences in the literature on electrical conductivity of ceria thin films of different degrees of disorder will affect ionic conductivity. The choice of organic solvent is, within precipitation-based thin-film processing, of strong relevance, affecting the ordering of a metal oxide.

For application of electrically conducting ceria-based thin films in MEMS it might be advantageous to use purely amorphous or even biphasic amorphous-crystalline microstructures. Such films show isotropic microstructures, low packing densities, and a high degree of disorder. Decreasing the glycol chain length allows for low-temperature deposition *via* a precipitation-based method of the thin-film and increases its degree of disorder through a high amount of space filling of organic residues within the metal oxide film. Purely amorphous electrically conducting functional thin films can be realized through the current processing conditions, as reported in this study, if their operation temperature is kept below 400 °C. Further studies will address the impact of structural disorder on the ionic and electronic conductivity of such precipitation-based thin films.

Acknowledgements

We thank Prof. Dr h.c. Joop Schoonman from Delft University of Technology for stimulating discussion. The project is part of the program 'Nanocrystalline ceramic thin films without sintering' (NANCER) funded by the Competence Center of Material Science and Technologies (CCMX), Switzerland.

References

1 J. L. M. Rupp and L. J. Gauckler, Microstructures and Electrical Conductivity of Nanocrystalline Ceria based Thin Films., *Solid State Ionics*, 2006, **177**, 2513.

2 P. Knauth and H. L. Tuller, Solute segregation, electrical properties and defect thermodynamics of nanocrystalline TiO_2 and CeO_2, *Solid State Ionics*, 2000, **136–137**, 1215–1224.

3 D. Beckel, A. Bieberle-Hutter, A. Harvey, A. Infortuna, U. P. Muecke, M. Prestat, J. L. M. Rupp and L. J. Gauckler, Thin Films for Micro Solid Oxide Fuel Cells, *J. Power Sources*, 2007, **173**(1), 325.

4 J. L. M. Rupp, A. Infortuna and L. J. Gauckler, Thermodynamic stability of gadolinia-doped ceria thin film electrolytes for micro-solid oxide fuel cells, *J. Am. Ceram. Soc.*, 2007, **90**(6), 1792–1797.

5 H. L. Tuller, Ionic conduction in nanocrystalline materials, *Solid State Ionics*, 2000, **131**(1–2), 143–157.

6 J. Musil, Baroch, J. Vlcek, K. H. Nam and J. G. Han, Reactive magnetron sputtering of thin films: present status and trends, *Thin Solid Films*, 2005, **475**(1–2), 208–218.

7 T. P. Niesen and M. R. De Guire, Review: deposition of ceramic thin films at low temperatures from aqueous solutions, *Solid State Ionics*, 2002, **151**(1–4), 61–68.

8 P. S. Patil, Versatility of chemical spray pyrolysis technique, *Mater. Chem. Phys.*, 1999, **59**(3), 185–198.

9 A. Evans, A. Bieberle-Hütter, J. L. M. Rupp and L. J. Gauckler, Review on microfabricated micro-solid oxide fuel cell membranes, *J. Power Sources*, 2009, **194**(1), 119–129.

10 R. M. Waser, Microstructure of ceramic thin films, *Curr. Opin. Solid State Mater. Sci.*, 1996, **1**(5), 706–714.

11 H. L. Tuller and R. Mlcak, Inorganic sensors utilizing MEMS and microelectronic technologies, *Curr. Opin. Solid State Mater. Sci.*, 1998, **3**(5), 501–504.

12 P. Muralt, K. H. J. Buschow, W. C. Robert, C. F. Merton, I. Bernard, J. K. Edward, M. Subhash and V. Patrick, Piezoelectric Thin Films for MEMS, in *Encyclopedia of Materials: Science and Technology*, Elsevier, Oxford, 2001, pp. 6999–7008.

13 U. P. Muecke, D. Beckel, A. Bernard, A. Bieberle-Hütter, S. Graf, A. Infortuna, J. L. M. Rupp, J. Schneider, P. Müller and J. Gauckler, Micro Solid Oxide Fuel Cells on a Glass Ceramic Substrate, *Adv. Funct. Mater.*, 2008, **18**(20), 3158.

14 A. Evans, A. Bieberle-Hütter, H. Galinski, J. L. M. Rupp, T. Ryll, S. Barbara, R. Tölke and L. J. Gauckler, Micro-solid oxide fuel cells: status, challenges, and chances, *Monatsh. Chem.*, 2009, **140**(9), 975.

15 J. L. M. Rupp, T. Drobek, A. Rossi and L. J. Gauckler, Chemical analysis of spray pyrolysis gadolinia-doped ceria electrolyte thin films for solid oxide fuel cells, *Chem. Mater.*, 2007, **19**(5), 1134–1142.

16 D. J. Chesnut, D. Hargman, P. J. Zapf, R. P. Hammond, R. LaDuca, R. C. Haushalter and J. Zubieta, Organic/inorganic composite materials: the roles of organoamine ligands in the design of inorganic solids, *Coord. Chem. Rev.*, 1999, **190–192**, 737–769.

17 P. Van Der Sluis and J. Kroon, Solvents and X-ray crystallography, *J. Cryst. Growth*, 1989, **97**(3–4), 645–656.

18 C. H. Gorbitz and H. P. Hersleth, On the inclusion of solvent molecules in the crystal structures of organic compounds, *Acta Crystallogr., Sect. B: Struct. Sci.*, 2000, **56**, 526–534.

19 P. van der Sluis, A. M. F. Hezemans and J. Kroon, Computer knowledge base for crystallization, *J. Cryst. Growth*, 1991, **108**(3–4), 719–727.

20 H. S. Kang, Y. C. Kang, H. Y. Koo, S. H. Ju, D. Y. Kim, S. K. Hong, J. R. Sohn, K. Y. Jung and S. B. Park, Nano-sized ceria particles prepared by spray pyrolysis using polymeric precursor solution, *Mater. Sci. Eng., B*, 2006, **127**(2–3), 99–104.

21 B. Ksapabutr, E. Gulari and S. Wongkasemjit, Sol–gel derived porous ceria powders using cerium glycolate complex as precursor, *Mater. Chem. Phys.*, 2006, **99**(2–3), 318–324.

22 C.-W. Kuo, Y.-H. Lee, I. M. Hung, M.-C. Wang, S.-B. Wen, K.-Z. Fung and C.-J. Shih, Crystallization kinetics and growth mechanism of 8 mol% yttria-stabilized zirconia (8YSZ) nanopowders prepared by a sol–gel process, *J. Alloys Compd.*, 2008, **453**(1–2), 470–475.

23 S. Ramanathan, R. V. Muraleedharan, S. K. Roy and P. K. K. Nayar, Dehydration and crystallization kinetics of zirconia-yttria gels, *J. Am. Ceram. Soc.*, 1995, **78**(2), 429–432.

24 J. L. M. Rupp, B. Scherrer, A. Harvey and L. J. Gauckler, Crystallization and Grain Growth Kinetics for Precipitation-based Ceramics: A Case Study on Amorphous Ceria Thin Films from Spray Pyrolysis, *Advanced Functional Materials*, 2009, **19**(1), 1–10.

25 J. L. M. Rupp, B. Scherrer and L. J. Gauckler, TTT-(Time-Temperature-Transformation) Diagrams for Crystallization of Metal Oxide Thin Films, *Advanced Functional Materials*, 2010, DOI: 10.1002/adfm.20100377.

26 J. L. M. Rupp, A. Infortuna and L. J. Gauckler, Microstrain and self-limited grain growth in nanocrystalline ceria ceramics, *Acta Mater.*, 2006, **54**(7), 1721–1730.

27 J. L. M. Rupp, C. Solenthaler, P. Gasser, U. P. Muecke and L. J. Gauckler, Crystallization of amorphous ceria solid solutions, *Acta Mater.*, 2007, **55**(10), 3505–3512.

28 S. Mishra, Anhydrous scandium, yttrium, lanthanide and actinide halide complexes with neutral oxygen and nitrogen donor ligands, *Coord. Chem. Rev.*, 2008, **252**(18–20), 1996–2025.

29 U. P. Muecke, G. L. Messing and L. J. Gauckler, The Leidenfrost effect during spray pyrolysis of nickel oxide-gadolinia doped ceria composite thin films, *Thin Solid Films*, 2009, **517**(5), 1515–1521.

30 U. P. Muecke, N. Luechinger, L. Schlagenhauf and L. J. Gauckler, Initial stages of deposition and film formation during spray pyrolysis—Nickel oxide, cerium gadolinium oxide and mixtures thereof, *Thin Solid Films*, 2009, **517**(5), 1522–1529.

31 C. Michaelsen and M. Dahms, On the determination of nucleation and growth kinetics by calorimetry, *Thermochim. Acta*, 1996, **288**(1–2), 9–27.

32 C. N. J. Wagner and E. N. Aqua, X-ray diffraction study of imperfections in rhenium, *J. Less Common Met.*, 1965, **8**(1), 51–62.

33 P. Scherrer, Bestimmung der Grösse und der inneren Struktur von Kolloidteilchen mittels Röntgenstrahlen, *Nachrichten von der Königlichen Gesellschaft der Wissenschaft zu Göttingen: Mathematisch-physikalische Klasse*, 1918, **1**, 98–100.

34 A. J. C. Wilson, *X-ray Optics*, 1949, 5.

35 D. Beckel, A. Dubach, A. R. Studart and L. J. Gauckler, Spray Pyrolysis of LSCF Thin Film Cathodes, *J. of Electroceramics*, 2006, **16**(3).

36 K. A. Jackson, *Kinetic Processes*, 2004, Wiley-VCH Verlag Gmbh & KGaA, Weinheim, Germany, ch. 15.3, vol. 199.

37 J. Malek, S. Matsuda, A. Watanabe, T. Ikegami and T. Mitsuhashi, Crystallization kinetics of zirconia-yttria gels, *Thermochim. Acta*, 1995, **267**, 181–194.

38 A. Stukowski, J. Markmann, J. Weissmüller and K. Albe, Atomistic origin of microstrain broadening in diffraction data of nanocrystalline solids, *Acta Mater.*, 2009, **57**(5), 1648–1654.

39 W. H. Weber, K. C. Hass and J. R. McBride, Raman-study of CEO$_2$-2nd-order scattering, lattice-dynamics, and particle-size effects, *Phys. Rev. B: Condens. Matter*, 1993, **48**(1), 178–185.

40 J. R. McBride, K. C. Hass, B. D. Pondexter and W. H. Weber, Raman and X-ray studies on Ce1-xRExO$_2$-y, where RE = La, Pr, Nd, Eu, Gd, and Tb., *J. Appl. Phys.*, 1994, **74**(4).

41 Z. D. Dohcevic-Mitrovic, M. J. Scepanovic, M. U. Grujic-Brojcin, Z. V. Popovic, S. B. Boskovic, B. M. Matovic, M. V. Zinkevich and F. Aldinger, The size and strain effects on the Raman spectra of Ce1-xNdxO$_2$-[delta] (0 < = x < = 0.25) nanopowders, *Solid State Commun.*, 2006, **137**(7), 387–390.

42 K. Kamada, N. Enomoto and J. Hojo, Optimization of electrochemical synthesis conditions for dense and doped ceria thin films, *Electrochim. Acta*, 2009, **54**(27), 6996–7000.

43 B. Matovic, Z. Dohcevic-Mitrovic, M. Radovic, Z. Brankovic, G. Brankovic, S. Boskovic and Z. V. Popovic, Synthesis and characterization of ceria based nanometric powders, *J. Power Sources*, 2009, **193**(1), 146–149.

44 R. Q. Long, Y. P. Huang and H. L. Wan, Surface Oxygen Species Over Cerium Oxide and Their Reactivities with Methane and Ethane by Means of in situ Confocal Microprobe Raman Spectroscopy, *J. Raman Spectrosc.*, 1997, **28**, 29–32.

45 M. Kitajima, Defects in crystals studied by Raman scattering, *Crit. Rev. Solid State Mat. Sci.*, 1997, **22**(4), 275–349.

46 A. Martínez-Arias, D. Gamarra, M. Fernández-García, X. Q. Wang, J. C. Hanson and J. A. Rodriguez, Comparative study on redox properties of nanosized CeO$_2$ and CuO/CeO$_2$ under CO/O$_2$, *J. Catal.*, 2006, **240**(1), 1–7.

47 S. Damyanova, B. Pawelec, K. Arishtirova, M. V. M. Huerta and J. L. G. Fierro, Study of the surface and redox properties of ceria-zirconia oxides, *Appl. Catal., A*, 2008, **337**(1), 86–96.

48 F. Zhang, S. W. Chan, J. E. Spanier, E. Apak, Q. Jin, R. D. Robinson and I. P. Herman, Cerium oxide nanoparticles: Size-selective formation and structure analysis, *Appl. Phys. Lett.*, 2002, **80**(1), 127–129.

49 K. Krishna, A. Bueno-Lopez, M. Makkee and J. A. Moulijn, Potential rare earth modified CeO$_2$ catalysts for soot oxidation, *Appl. Catal., B*, 2007, **75**, 189.

50 I. Kosacki, T. Suzuki, H. U. Anderson and P. Colomban, Raman scattering and lattice defects in nanocrystalline CeO$_2$ thin films, *Solid State Ionics*, 2002, **149**(1-2), 99–105.

51 R. Gallage, A. Matsuo, T. Fujiwara, T. Watanabe, N. Matsushita and M. Yoshimura, Direct patterning of dense cerium oxide thin film by developed ink-jet deposition method at moderate temperatures, *Thin Solid Films*, 2009, **517**(16), 4515–4519.

52 J. E. Spanier, R. D. Robinson, F. Zheng, S. W. Chan and I. P. Herman, Size-dependent properties of CeO$_2$-y nanoparticles as studied by Raman scattering, *Phys. Rev. B: Condens. Matter Mater. Phys.*, 2001, **64**(24), 245407.

53 G. Gouadec and P. Colomban, Raman Spectroscopy of nanomaterials: How spectra relate to disorder, particle size and mechanical properties, *Prog. Cryst. Growth Charact. Mater.*, 2007, **53**(1), 1–56.

54 G. Gouadec and P. Colomban, Raman spectroscopy of nanostructures and nanosized materials, *J. Raman Spectrosc.*, 2007, **38**(6), 598–603.

55 S. Tsunekawa, R. Sivamohan, S. Ito, A. Kasuya and T. Fukuda, Structural studyon monosize CeO$_2$-x nano-particles, *Nanostruct. Mater.*, 1999, **11**(1), 141–147.

56 L. J. Wu, H. J. Wiesmann, A. R. Moodenbaugh, R. F. Klie, Y. M. Zhu, D. O. Welch and M. Suenaga, Oxidation state and lattice expansion of CeO$_2$-x nanoparticles as a function of particle size, *Phys. Rev. B: Condens. Matter Mater. Phys.*, 2004, **69**(12), 125415.

57 D. G. Georgiev, M. Mitkova, P. Boolchand, G. Brunklaus, H. Eckert and M. Micoulaut, Molecular structure, glass transition temperature variation, agglomeration theory, and network connectivity of binary P–Se glasses, *Phys. Rev. B: Condens. Matter Mater. Phys.*, 2001, **64**(13), 134204.